ACS APPLIED MATERIALS & INTERFACES

Research Article

www.acsami.org

Zeta Potential, Contact Angles, and AFM Imaging of Protein Conformation Adsorbed on Hybrid Nanocomposite Surfaces

Ana C. Pinho and Ana P. Piedade*

CEMUC-GNM, Department of Mechanical Engineering, University of Coimbra, Rua Luís Reis Santos, 3030-788 Coimbra, Portugal

ABSTRACT: The sputtering deposition of gold (Au) and poly(tetrafluoroethylene) (PTFE) was used to prepare a nanocomposite hybrid thin film suitable for protein adsorption while maintaining the native conformation of the biological material. The monolithic PTFE and the nanocomposite PTFE/Au thin films, with Au content up to 1 at %, were co-deposited by r.f. magnetron sputtering using argon as a discharge gas and deposited onto 316L stainless steel substrates, the most commonly used steel in biomaterials. The deposited thin films, before and after bovine serum albumin (BSA) adsorption, were thoroughly characterized with special emphasis on the surface properties/characteristics by atomic force microscopy (AFM), zeta potential, and static and dynamic contact angle measurements, in order to assess the relationship between structure and conformational changes. The influence of a pre-adsorbed peptide (RGD) was also evaluated. The nanotopographic and chemical changes induced by the presence of gold in the nanocomposite thin films enable RGD bonding, which is critical for the maintenance of the BSA native conformation after adsorption.

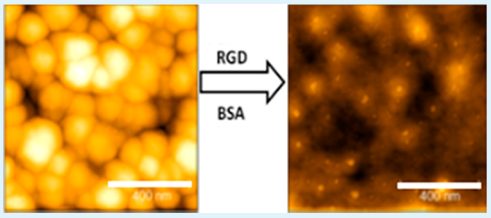

KEYWORDS: *nanocomposite, RGD, BSA, AFM, zeta potential, contact angle hysteresis*

INTRODUCTION

The concept of biocompatibility, as well as its definition, is in constant evolution. The need for specific and direct interactions between biomaterials and tissue components instead of the inertness of the "non-approach" first associated with implantable biomaterials has been recently demonstrated.[1] In fact, the biological events included in the injury response are also critical components involved in the promotion of a functional non-scar tissue. The improved outcome and constructive remodeling occur with a transition to a M2 macrophage phenotype, which always implies macrophage recruitment because of the host biological response in opposition to the concept of "inertness".[1]

One of the early events in the host response to implanted biomaterials is protein adsorption, which together with the surface chemistry and the topographic features of the material have been considered determinant factors in the foreign body response.[2−5] Many efforts have been focused on developing surfaces that are resistant to protein adsorption.[6,7] However, the adhesion of specific proteins such as human serum albumin inhibits thrombus formation.[8] In fact, as demonstrated by other authors, when a polymer surface was modified with BSA, the biocompatibility in terms of the reduction of thrombus formation, platelet adhesion, and hemolysis was improved when compared with the unmodified material.[9]

In the face of the recent developments of protein−biomaterials interaction, the challenge is designing surfaces that proactively interact with the biological host by being able to promote protein adhesion but without stimulating its loss of structural integrity. One of the approaches that researchers have followed is the modification of the surface with the incorporation of biomimetic materials, such as those that compose the extracellular matrix. In fact, cell−extracellular matrix adhesion provides anchorage cues for migration and signals for growth and differentiation. It has been known for some time that a number of adhesive proteins contain the arginine−glycine−aspartic acid (RGD) peptide and that this sequence is used by cell−surface proteins to recognize and bind their ligands, thus mediating cell adhesion.[10−12]

Moreover, metallic materials such as gold nanoparticles (AuNp) have been used as a support for the immobilization of RGD in several applications, including the detection of tumor specific sequences,[13] enhanced immobilization of human neural stem cells on gold electrodes,[14] or in drug delivery for the treatment of rheumatoid arthritis.[15] Along with these specific applications, AuNp have also been used in the development of nanocomposites, especially to promote nanotopographic features that induce cell proliferation and differentiation.[16] Furthermore, AuNp enable straightforward chemical surface modification that could further affect biological interaction.

The aim of this work was to develop polymeric surfaces that included Au of nanometric dimensions and to study their ability to promote protein adhesion without inducing denaturation. However, polymeric modification strategies that involve the treatment of the surface of bulk materials are known to suffer from aging, with a rather limited shelf live as the surface adaptation leads to the disappearance of the created chemical groups.[17] Consequently, the choice was to co-deposit PTFE and Au thin films by radiofrequency (r.f.) magnetron sputtering. The chemical modifications that the polymer suffers during the deposition process are permanent and can then be

Received: June 13, 2013
Accepted: July 30, 2013
Published: July 30, 2013

Table 1. Designation, Chemical Composition, and Thickness of the Deposited Thin Films

designation	chemical composition (at %)				thickness (nm)
	C	O	F	Au	
PTFE	56.8 ± 1.2	0.3 ± 0.01	42.9 ± 0.7	–	1340–1390
PTFE 0.6	56.5 ± 1.7	0.3 ± 0.01	42.6 ± 1.0	0.6 ± 0.01	1100–1200
PTFE 0.7	56.3 ± 0.9	0.2 ± 0.01	42.8 ± 1.1	0.7 ± 0.01	960–1050
PTFE 1	55.8 ± 1.0	0.3 ± 0.01	43.0 ± 0.8	1.0 ± 0.02	1240–1310

related to the protein adsorption behavior. Moreover, the used technique allows for obtaining metastable materials that cannot be synthetized by conventional techniques. For surfaces intended for biomedical applications, sputtering presents as an additional advantage the fact that the surfaces are sterilized after the deposition process. This enables avoiding further processing that can induce changes on the surface properties, such as structural changes triggered by the autoclave procedure.

EXPERIMENTAL SECTION

Deposition Technique. All reagents and materials were purchased from commercial sources and were used as received, unless otherwise stated. The monolithic PTFE and hybrid PTFE/Au thin films were sputter-deposited using a radiofrequency (r.f.) power supply of 1000 and 500 W, branched to the two assisted magnetron targets and substrate holder, respectively. PTFE (99.999%) and Au (99.999%) targets of 100 mm in diameter were used. The deposition parameters were 1×10^{-4} Pa ultimate vacuum pressure, 3.2 W cm^{-2} discharge power density for PTFE and from 0 to 1.6 W cm^{-2} for Au, 0.7 Pa total discharge pressure, and 10 min deposition time. The thin films were deposited onto glass lamellae (Ra = 0.002 μm) and AISI stainless steel 316L substrates (316L). The metallic material was polished with SiC paper grit down to 2500 and with 1 μm grain size diamond paste to Ra = 0.02 μm.

Characterization Techniques. The chemical composition of all surfaces was assessed by electron probe micro-analysis (EPMA) using Camebax SX 50 equipment operating at 5 kV and 60 nA, after optimizing the quantification procedure. Chemical functional groups of the modified surfaces were identified with a Jasco FTIR-4200 Mk II equipped with an attenuated total reflectance accessory. The infrared spectra were recorded at 4 cm^{-1} spectral resolution and accumulation of 168 interferograms. The presented spectra were obtained after subtracting the substrate data to the thin film spectra.

The XRD spectra were obtained using a Philips X'Pert with Co radiation ($\lambda k\alpha 1$ = 0.178896 nm and $\lambda k\alpha 2$ = 0.179285 nm), a collimated detector, and Bragg–Brentano geometry. All the tests were performed with a step size of 0.025° and a time per step of 0.5 s. Transmission electron microscopy (TEM) studies were performed on a Tecnai G2 microscope. The samples were cut from a coated 316L AISI stainless steel thin foil with a 0.1 mm thickness, electro eroded, and finally thinned by ion milling in a Gatan Duo Ion Mill 600DIF.

The mechanical properties were determined by nanoindentation performed using the micro materials nanotest system in the load control mode. Loads of 0.30 mN were applied on the thin films deposited on AISI 316L stainless steel. The method for obtaining the hardness (H) and Young's modulus (E) from the loading/unloading curves has already been described elsewhere.[18,19] The load rate was tuned so that each test would last about 30 s, with a 5 s hold period at the maximum load and a 30 s hold period during unloading at 10% of the maximum load for thermal drift correction. A minimum of 25 indentations were performed at each maximum load using a Berkovich indenter. The β factor used was 1.034, and the function area = $A + Bhc + Chc^2$ where A, B, and C are variables that were calculated from the calibration tests with a fused silica standard with a hardness of 8.8 GPa and a Young's modulus of 72 GPa.

All AFM imaging was performed in air using a diInnova—Veeco atomic force microscope (Bruker, U.S.A.) operated in tapping mode. A silicon aluminum-coated probe of 320 kHz resonance frequency (f_0) and 40 N m^{-1} spring constant (k) (Bruker) were used. All images (512 samples/line × 512 lines) were taken at room temperature, and the images and surface roughness are representative of at least five measurements taken over different locations on the surfaces. This technique was also used to evaluate thin film thickness. The wettability characteristics of thin films were assessed by measuring the static contact angle of the surfaces with 10 μL of distilled and deionized water, formamide, and diiodomethane in a DataPhysics QCA-20 apparatus. For each sample, a minimum of seven measurements was taken, after allowing the system (air–water–surface) to reach equilibrium, and the average value calculated. The values of the contact angles were used to calculate the water adhesion tension τ^0, with $\tau^0 = \gamma_0 \cos\theta$, where γ_0 is the surface tension of pure water, and θ is the contact angle value. The contact angle values were also used to determine the surface tension γ_S as the sum of its polar, γ_S^p, and dispersive, γ_S^d, components according to previously described procedure.[20] The hysteresis of the dynamic contact angle ($H\theta$) was determined by the maximal difference between advancing, θa, and receding angles, θr, for a volume of 10 μL. The quantification of these angles was done using the add/remove volume method. Water was continuously added onto the surface until reaching a volume of 100 μL (advancing) and after complete removal (receding). The surface charge was determined in a SurPASS, Anton Paar, GmbH, using the adjustable gap cell. The measurements were made using two different solutions: 1 mM phosphate saline solution (PSS) and 1 mM KCl at pH 7.4. To determine the isoelectric point of each surface, the pH of the solutions varied from 3 to 10 by automatic direct titration with HCl and NaOH 0.1 M solutions.

In the interaction with bovine serum albumin (BSA), the study also assessed the influence of the immobilization of the RGD peptide previous to BSA exposure. The peptide used was a 11-mer with four cysteine residues, RGD-4C. The modified and unmodified 316L surfaces were placed in a 1.5 mL RGD solution (0.5 mg mL^{-1} in 0.1 M phosphate buffer at pH 7.4) for 2 h at 20 °C. After being thoroughly washed with sterile Milli-Q water, these samples and their parallels without RGD were placed in 2 mL of BSA solution (4 mg mL^{-1} in 0.1 M phosphate buffer at pH 7.4) for 18 h at 4 °C. The concentration of BSA was chosen in order to be able to image separate protein molecules by AFM. The amount of total immobilized protein was calculated using the Bradford reagent against a standard BSA calibration curve.

RESULTS AND DISCUSSION

The results of chemical composition, thickness, and designation of the deposited thin films are present in Table 1. The chemical composition indicates that, as expected, the thin films present a loss of fluorine when compared with the bulk target material. This is a known fact for sputter-deposited thin films from PTFE targets, and it is due to the chemical rearrangement of the ejected molecular species. The plasma characteristics induce the deposition of short and reticulated chains with unsaturated bonds.[21] The Au content on the hybrid thin films is very low and does not present any relation with the deposition power. This can be due to the configuration of the substrate holder regarding the deposition targets. In fact, due to the high sputtering yield of Au (2.5 atoms/ion), the substrate holder was placed directly over the polymeric target in order to avoid high metal concentrations, and the deposition was made without substrate rotation. This configuration is known to decrease the

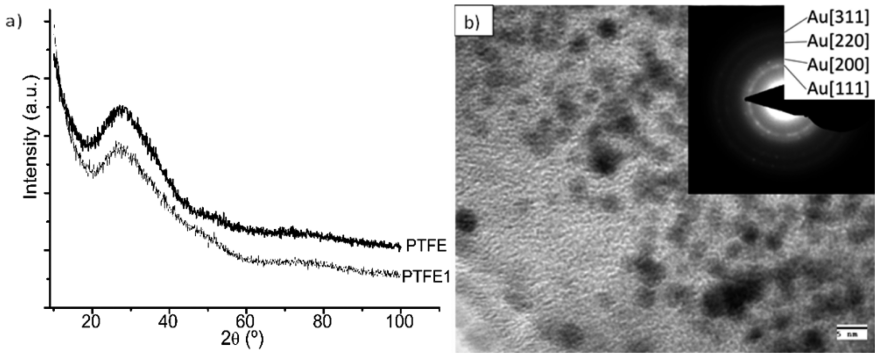

Figure 1. (a) Diffractograms of PTFE and PTFE 1 thin films and (b) a PTFE 1 representative TEM bright field image with insert of electron diffraction pattern (bar = 5 nm).

metallic content on the polymeric matrix in mixed targets, thus implying that by using the described configuration, the Au content will decrease even further.[22] The chosen strategy can also justify the fact that monolithic PTFE film is thicker than the hybrid ones.

The structural analysis by XRD shows that, as described in the literature,[21] the sputtered PTFE always present a lack of structural order, and they are of amorphous nature (Figure 1a). As the content of the metallic element is not sufficient to unambiguoulys identify the structural differences between monolithic and hybrid thin films, TEM analysis was performed (Figure 1b). This technique allowed underlining the amorphous nature of the PTFE matrix and simultaneously identifies the presence of gold particles of nanometric dimension, revealing the nanocomposite nature of the hybrid deposited thin films. The microstructural characterization also allowed confirming that the gold nanoparticles are homogeneously dispersed on the polymeric matrix.

The mechanical properties of all the thin films were assessed, and the results of the two most different surfaces are present in Table 2. The hardness values are very similar with the nanocomposite film exhibiting a slightly lower value. This fact is due to the incorporation of a ductile material, gold, although the observed decrease is small, as a consequence of its low content. The Young's modulus, unlike hardness, is highly dependent on the chemical composition and chemical bonds. The incorporation of the metallic element, besides changing the chemical composition, seems to be responsible for the presence of new chemical bonds

Table 2. Mechanical Properties of PTFE and PTFE 1 Determined by Nanoindentation

	mechanical properties	
designation	hardness (H) (GPa)	Young's modulus (E) (GPa)
PTFE	0.66 ± 0.13	5.20 ± 0.77
PTFE 1	0.61 ± 0.04	6.24 ± 0.27

Considering the application for biomedical implants, it is necessary that the surfaces present low friction coefficients. In fact, it has been established that friction will decrease with an increase in Young's modulus if the direction of minimum shear resistance can be maintained parallel to the substrate.[22] Thus, within the developed surfaces, PTFE 1 thin film corresponds to these premises, indicating that it possesses the appropriate mechanical properties.

The surface topography of the modified surfaces was evaluated by AFM. All the PTFE/Au thin films present a higher nucleation density when compared with PTFE coating as exemplified in Figure 2. Also, the peak/valley height is more pronounced in the film of PTFE due to particle coalescing into larger aggregates. In fact, the AFM images were treated using "Gwyddion" software by applying the "watershed" mask, which enabled the calculation of average particle size (Table 3). The same program also allowed determining the average surface roughness, S_a, and the surface mean square roughness, S_m.[23] Both particle size and surface roughness parameters are, as expected, very similar for the hybrid nanocomposite thin films and inferior to the PTFE coating (Table 3). Therefore, inclusion of Au leads to a higher density of nucleation by depositing preferentially in the particle boundary and "inhibiting" the coalescence of the polymeric agglomerates contributing to smaller particle dimension and lower surface roughness.[24] This feature is clearly visible in the phase image of the PTFE 1 surface where, besides the nanometric dimensions of the metallic element, it is manifest its distribution surrounding the polymeric particles. Also, this characterization reinforces the observations made by TEM highlighting the fact that the metallic nanoparticles are well dispersed both in the surface and within the thickness of the coating.

Bulk PTFE is a polymer with high structural order that results in well-resolved FTIR spectra. Therefore, PTFE-based thin films, because of their amorphous nature, present FTIR spectra with wider and poor defined peaks (Figure 3). To correctly identify functional chemical groups, a deconvolution of each spectrum was performed, and the quantification of each band presented as the area of interest divided by the area in the range of the characteristic PTFE chemical groups (1000−1400 cm^{-1}), resulting in a relative quantification[25,26] that enables the comparison between the different coatings (Table 4). According to the calculations, it is possible to conclude that in all the modified surfaces the major contribution of functional chemical groups with hydrophilic character is given by hydroxyl groups (−OH) (2900−3500 cm^{-1}). Moreover, the percentage of −OH groups in the hybrid thin films are higher than those calculated for the polymeric coating, increasing with the augmentation of the metallic content.

Simultaneously, the percentage of CF_3 groups (980 cm^{-1}) normally associated with termination of the polymeric chains also increases with the amount the metallic element. Therefore, deposition conditions that induce a higher percentage of shorter chains are also responsible, in the chosen hybrid system, for the increased incorporation of hydroxyl groups. In fact, the

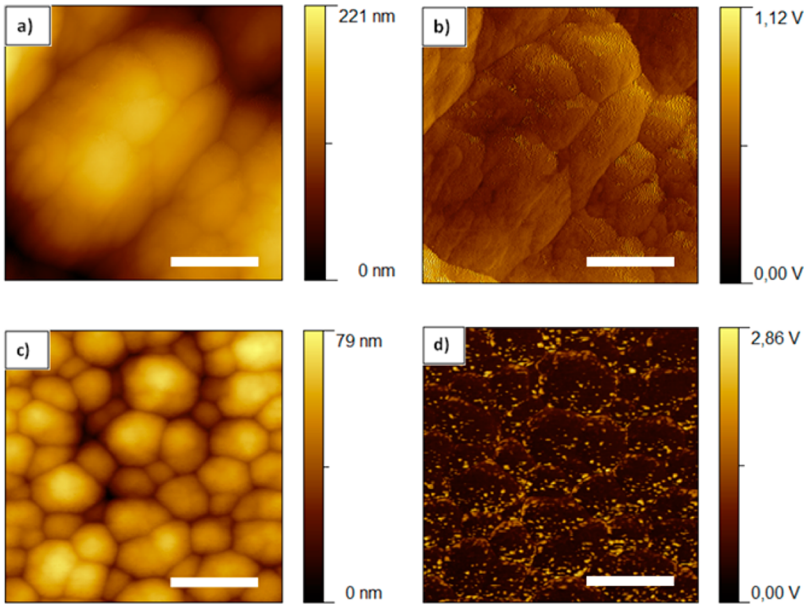

Figure 2. AFM imaging of (a, b) PTFE and (c, d) PTFE 1 surfaces. (a, c) Topographic and (b, d) phase images correspond to a 1 μm × 1 μm area (bar = 400 nm).

Table 3. Average and Standard Deviation Values of Polymeric Particle Size and Surface Roughness Parameters, Determined by AFM

surface	particle size (nm)	S_a (nm)	S_{ms} (nm)
PTFE	235 ± 22	41.2 ± 0.7	50.9 ± 1.3
PTFE 0.6	100 ± 14	10.6 ± 0.4	13.2 ± 0.9
PTFE 0.7	89 ± 14	13.2 ± 0.3	16.9 ± 1.0
PTFE 1	116 ± 12	11.1 ± 0.4	14.0 ± 0.7

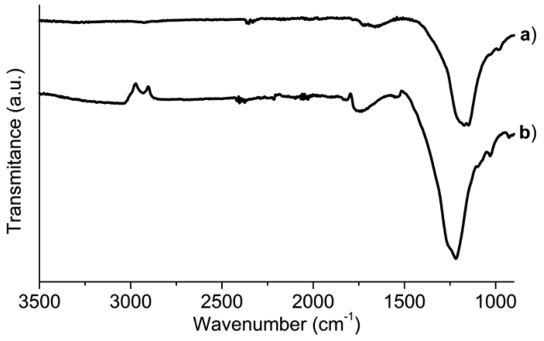

Figure 3. FTIR spectra of (a) PTFE and (b) PTFE 1 thin films.

Table 4. Relative Quantification of Two Absorption Bands Evaluated from FTIR Spectra

	relative quantification (%)			
wavenumber (cm^{-1})	PTFE	PTFE 0.6	PTFE 0.7	PTFE 1
980 ($-CF_3$)	0.5	0.7	1.5	36.8
2900−3500 (−OH)	3.2	14.2	16.2	38.4

shorter the polymeric chains the higher the percentage of dangling bonds, which due to their chemical reactivity rapidly tend to stabilize by creating covalent bonds with other chemical groups, such as −OH. This new type of chemical bond also contributes to the increase in Young's modulus as indicated in the mechanical characterization of the modified surfaces.

The wettability characteristics of all surfaces were assessed through contact angle measurements (Table 5). All surfaces are considered hydrophobic, $\theta_{water} > 65°$, and present a tendency to decrease the contact angle with the presence of Au. Although this trend is consistent with the presence of −OH groups, this fact does not imply that the surfaces can be considered hydrophilic; the contact angles with water are always above 100°, which is characteristic of hydrophobic surfaces. Even though the surface roughness critically influences the measurement of the contact angles, the similar values of the S_a values of hybrid nanocomposite thin films allows establishing the difference between them as the result of the chemical composition.

The critical wetting tension (γ_c) was calculated using Zisman's plots, and the determined values (Table 5) present a correlation with the content of Au. In fact, the PTFE thin film has a critical wetting tension very similar to that of bulk PTFE (19 mJ m^{-2}), which indicates the presence of very small contents of chemical groups with hydrophilic characteristics. As the Au content increases, γc also increases, although not abruptly as the Au content in the thin films is very low. This fact is highlighted by the determination of the surface energy of the modified surfaces (Table 5), in particular by the polar component, γ_S^P, which strongly contributes to the wettability of the surfaces and is directly related to the presence of hydrophilic functional chemical groups on the surface as reported in other studies.[20]

However, some authors[27,28] consider that the parameter that truly relates the wetabillity characteristics of a surface with its performance as a biomaterial is the water adhesion tension, τ^0, which is calculated by the product of water tension γ_0 (72.8 mJ m^{-2}) by the cosine of the static contact angle between water and the surface. These researchers consider that this is the only parameter that takes in consideration the biophysical role of water at a biomaterial surface. All surfaces present τ^0 values (Table 4) below the Berg's limit (τ^0 = 30 mJ m^{-2}), which means they are able to support protein adsorption without triggering the coagulation cascade.[28] In fact, protein adsorption on hydrophilic surfaces is thermodynamically hindered.[27] The

dx.doi.org/10.1021/am402302r | ACS Appl. Mater. Interfaces 2013, 5, 8187−8194

Table 5. Contact Angles, Critical Wetting Tension, Surface Energy, and Water Adhesion Tension Values of the Deposited Thin Films

	contact angle (deg)				surface energy (mJ m^{-2})			
surface	water	form[a]	dii[b]	γ_c (mJ m^{-2})	γ_s^d	γ_s^p	γ_s	τ^0 (mJ m^{-2})
PTFE	126 ± 6	108 ± 2	77 ± 3	20.0	2.0	0.1	2.1	−42.9
PTFE 0.6	106 ± 4	93 ± 4	84 ± 3	24.0	2.2	1.5	3.7	−20.4
PTFE 0.7	102 ± 2	92 ± 2	77 ± 2	25.5	3.4	1.6	5.0	−16.0
PTFE 1	102 ± 3	88 ± 4	75 ± 2	26.4	4.3	2.0	6.3	−15.3

[a]Formamide. [b]Diiodomethane.

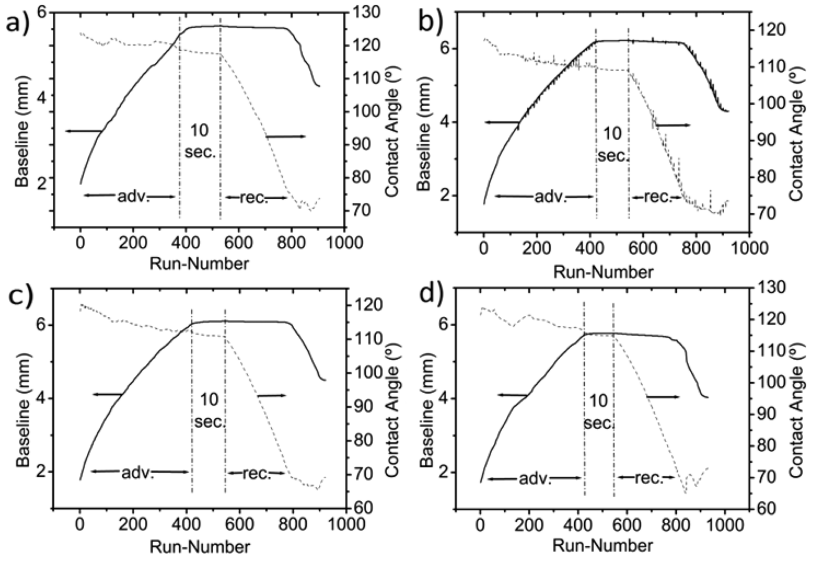

Figure 4. Variation in the baseline water−surface and of the contact angle during the advancing and receding steps of the dynamic determination of contact angle hysteresis: (a) PTFE, (b) PTFE 0.6, (c) PTFE 0.7, and (d) PTFE 1.

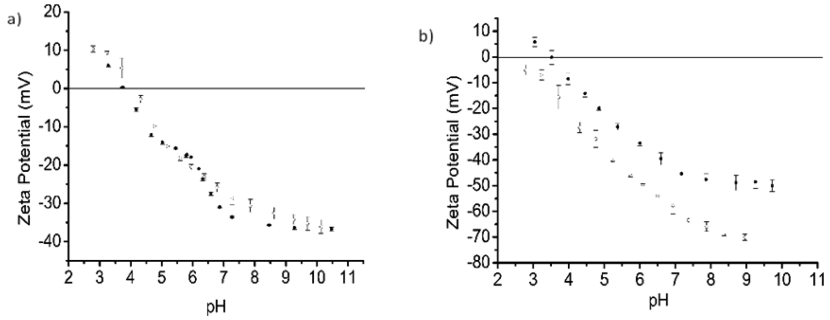

Figure 5. Variation in the zeta potential values with pH tested in two electrolytes: (a) KCl 1 mM and (b) PSS 1 mM (closed squares, PTFE; open squares, PTFE 1).

activation energy necessary to disrupt the three-dimensional water network formed on the surface of hydrophilic materials constitutes a barrier in static conditions.

Considering that the modified surfaces are intended to be used into the human body and therefore constantly immersed in biological fluid, one of the aspects investigated was their performance once they are wetted. For this reason, the hysteresis (H_θ) of the contact angle, calculated as the major difference between advancing (θ_a) and receding angles (θ_r) with water, was studied by the adding/removing liquid method. All the surfaces present $H\theta$ values around 50°, which is macroscopic evidence of the existence of hydrophobic/hydrophilic regions on the surface.[29] This fact highlights that the −OH groups content is low (as expected from the static contact angle measurements) and is not uniformly distributed on the surface. By presenting the data of the variation of the contact angle together with the diameter of the water−surface interaction (baseline), it is easier to understand what is involved (Figure 4).

During the advancing angle stage, the contact angle values remain without major changes because the baseline increases with increasing drop volume, indicating that no instant interaction with the liquid occurs, thus allowing its free spreading. However, after the 10 s delay, during the receding stage, the drop volume decreases, but the baseline remains constant. This indicates that the hydrophilic surface domains interact with water and retain the drainage caused by a decreased volume of the drop, which by maintaining the baseline constant causes a decrease in the contact angle.[30,31] The film PTFE 1 is the one that presents the lower contact

angle immediately before the baseline begins to decrease due to the presence of hydroxyl groups. This implies that once the surfaces are implanted, and therefore wetted by the biological fluids, the interaction of the biological species is slightly favored due to the chemical interactions. This fact in addition to the overall hydrophobic characteristic of the surface provides an environment that can be considered appropriate for protein adsorption.

The surface zeta potential study was performed using KCl and PSS 1 mM solutions as electrolytes and was determined for pH values between 3 and 10 (Figure 5). It is expected that different chemical composition influences the conductivity of the solutions and therefore the zeta potential. In fact, the zeta potentials at physiological pH of samples PTFE and PTFE 1 is similar ($\cong -30$ mV) when determined in KCl electrolyte, and, in this electrolyte, the isoelectric point (IEP) occurs for both surfaces at pH 3.5 (Figure 5a). When PSS was used, the zeta potential values at physiological pH were −45 mV for PTFE and −65 mV for PTFE 1, and it was not possible to determine the IEP of the latest surface, whereas the monolithic polymeric film presents the same IEP value determined with KCl (Figure 5b). The different behavior is due to the valence of the ions of the electrolyte solutions, which influence the thickness of the double layer because the higher the valence of the ions the smaller the width of the double layer.[32] Therefore, the electrolyte with a higher difference of valence of its ions (PSS) is the electrolyte that induces lower values of zeta potential. The difference between PTFE and PTFE 1 in PSS is explained by the presence of −OH groups. In fact, other studies have demonstrated that the chemical nature of the groups that are responsible for different wetabillity behaviors is related with surface charge; whereas $-NH_2$ terminated surfaces exhibit an almost neutral surface charge, −OH containing groups (such as −COOH) present negative surface charge.[33] Furthermore, using the electrolyte similar to the biological fluids of all surfaces present at physiological pH surface charge values outside the designated "unstable range" (from −30 to +30 mV), which are considered undesirable for biomedical applications.[32]

It is known from the literature that surfaces with larger surface area adsorb more protein and that a large surface is correlated with an increased surface roughness.[34] In fact, a PTFE surface has higher Sa and Sms values and adsorbs larger amounts of BSA (Table 6) as it corresponds to surfaces with

Table 6. Quantification of Adsorbed Protein, Surface Charge, and Contact Angle on PTFE and PTFE 1 Surfaces, with and without Pre-Adsorbed RGD

		after protein adsorption	
surface	adsorbed protein (μg mm^{-2})	contact angle (deg)	surface charge (mV)
PTFE + BSA	0.2 ± 0.01	44 ± 9	−7 ± 3
PTFE + RGD + BSA	18.0 ± 0.20	62 ± 1	−10 ± 2
PTFE 1 + BSA	0.4 ± 0.01	44 ± 3	−41 ± 4
PTFE 1 + RGD + BSA	14.0 ± 0.15	68 ± 9	−29 ± 5

capacities to accommodate more nanometric protein molecules per macroscopic area when compared with surface with lower surface areas. In fact, BSA is, in its native state, a globular protein with dimensions varying between 15 and 5 nm.[35] Moreover, the pre-adsorption of RGD is favorable on the bonding of BSA. However, as recently demonstrated by several authors, the compatibility of biomaterial surfaces should be based on "the ability of surfaces to maximally retain the native state of proteins as opposed to focusing merely on the amount of protein that is adsorbed.[36,37]

In fact, and although the amount of BSA in the PTFE thin film with RGD is slightly higher than the content in the PTFE 1 surface, it is known that RGD readily forms covalent bonds to the Au through the free thiol on cysteine residues,[6] whereas its binding to sputtered PTFE is through weak physiosorption to the polymer surface. Also, the residual values of protein adsorption on the surface without pre-adsorbed RGD demonstrate that the repulsive electrostatic forces between the negative surface and protein overcome the hydrophobic attraction.[38] These facts are expressed by the different contact angles and zeta potential values of the surfaces after protein adsorption (Table 6). The surfaces with pre-adsorbed RGD present similar contact angle values that are higher than those exhibited by the surfaces with no peptide, indicating differences upon the chemical groups exposed to the interface with water. Additionally, it is know that BSA presents a IEP at pH 4.8,[38] which implies a negative surface charge of −20 mV at physiological pH,[39] which is attributed to the surface charge of domains I and II of BSA that correspond to the domains that are exposed when the protein in its native conformation.[40] Upon denaturation, domain III is exposed and presents a zeta potential value of −1.3 mV.[40] The surface charge of the PTFE + RGD + BSA surface indicates that in some extent the domain III of BSA is exposed in opposition with the hybrid nanocomposite thin film, where the value around −30 mV corresponds to a less negative value than the surface exhibit before protein adsorption and very close to the value of the native protein. This observation indicates an almost complete coverage of the surface with the protein and that BSA preserves its native configuration.

To confirm this possibility, we obtained AFM images of both PTFE and PTFE 1 surfaces after adsorption of RGD and BSA (Figure 6).

The obtained results allowed establishing that the topographic differences between the two surfaces are essentially the globular features displayed by the PTFE 1 surface (Figure 6c,d), which correspond to the dimensions (Figure 6e) of the globular native BSA adsorbed with "side-on" orientation.[35] In contrast, the surface of PTFE does not present any distinctive topographies and does reinforce the idea that the adsorption process on this surface induces the loss of native conformation.

The surface characterization before and after protein adsorption, without RGD pre-treatment, indicate that as both the protein and the surface are negatively charged the adsorption should be mainly driven by hydrophobic interactions.[41] In this case, a slight increase in BSA adsorption should be quantified in PTFE surface. As this was not observed in this work, it indicates that the repulsive electrostatic forces overcome the wetabillity factor as previously stated.

After RGD treatment, the peptide is covalently bond to the surface of PTFE 1 and physiosorbed onto the PTFE surface. This fact is responsible for the conformation of the BSA molecules. In fact, when RGD is covalently bound to the surface through thiol groups, no conformational changes of the peptide can occur, thus providing a constant anchorage environment for the protein attachment. When the RGD adsorption occurs only by phisiosorption, the presence of albumin can dislocate the pre-adsorbed peptide inducing the interaction of hydrophobic domains of the protein with the

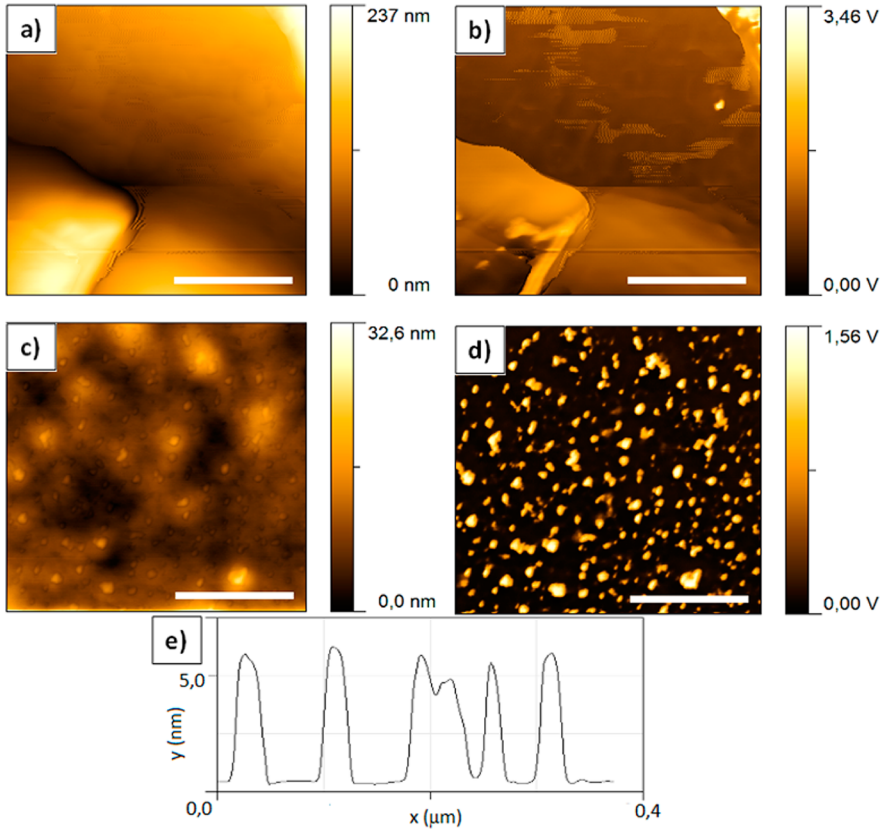

Figure 6. AFM imaging of (a, b) PTFE + RGD + BSA and (c, d) PTFE 1 + RGD + BSA surfaces. (a, c) Topographic and (b, d) phase images (bar = 400 nm) and (e) roughness profile of a section of image c.

surface suggesting that the adsorbed protein molecules change their conformation to spread over the surface.[42]

CONCLUSION

Nanocomposite hydrid thin films were successfully obtained by r.f. magnetron co-deposition from PTFE and Au targets. The incorporation of small amounts of Au (up to 1 at %) is responsible for the changes in nanotopography, introduction of some hydroxyl groups, and bonding sites for the thiol residues of both RGD peptide and BSA protein. The pre-adsorption of RGD provides an extra cellular type environment that is responsible for the maintenance of the BSA apparent native structure after adsorption on the nanocomposite thin films, according to zeta potential and contact angle values and AFM images. The results of this study open new insights on the surface tailoring of biomaterials surfaces in order to promote a proactive interaction with the biological systems but without triggering adverse pathways that led to implant rejection.

AUTHOR INFORMATION

Corresponding Author

*E-mail: ana.piedade@dem.uc.pt.

Author Contributions

The manuscript was written through contributions of all authors. All authors have given approval to the final version of the manuscript and contributed equally.

Notes

The authors declare no competing financial interest.

ACKNOWLEDGMENTS

This research is sponsored by FEDER funds through the program COMPETE, Programa Operacional Factores de Competitividade, and by national funds through FCT, Fundação para a Ciência e a Tecnologia, under projects PEst-C/EME/UI0285/2013 and CENTRO-07-0224-FEDER-002001.

REFERENCES

(1) Brown, B. M.; Badylak, S. F. *Acta Biomater.* **2013**, *9*, 4948−4955.
(2) Brodbeck, W. G.; Nakayama, Y.; Matsuda, T.; Colton, E.; Ziats, N. P.; Anderson, J. M. *Cytokine+* **2002**, *18*, 311−319.
(3) Kou, P. M.; Pallansana, N.; Bowden, R.; Cunningham, B.; Joy, A.; Kohn, J.; Babensee, J. E. *Biomaterials* **2012**, *33*, 1699−1713.
(4) Lee, S.; Choi, J.; Shin, S.; Im, Y. M.; Song, J.; Kang, S. S.; Nam, T. H.; Webster, T. J.; Kim, S. H.; Khang, D. *Acta Biomater.* **2011**, *7*, 2337−2344.
(5) Chen, S.; Jones, J. A.; Xu, Y.; Low, H. Y.; Anderson, J. M.; Leong, K. W. *Biomaterials* **2010**, *31*, 3479−3491.
(6) Hasebe, T.; Yohena, S.; Kamijo, A.; Okazaki, Y.; Hotta, A.; Takahashi, K.; Suzuki, T. *J. Biomed. Mater. Res.* **2007**, *83A*, 1192−1199.
(7) Vandencasteele, N.; Nisol, B.; Viville, P.; Lazzaroni, R.; Castner, D. G.; Reniers, F. *Plasma Process. Polym.* **2008**, *5*, 661−671.
(8) Lousinian, S.; Logothetidis, S. *Microelectron. Eng.* **2007**, *84*, 479−485.
(9) Khan, W.; Kapoor, M.; Kumar, N. *Acta Biomater.* **2007**, *3*, 541−549.
(10) Hersel, U.; Dahmen, C.; Kessler, H. *Biomaterials* **2003**, *24*, 4385−4415.
(11) Ruoslahti, E.; Pierschbacher, M. D. *Cell* **1986**, *44*, 517−518.
(12) Benoit, Y. D.; Groulx, J. F.; Gagné, D.; Beaulieu, J. F. *J. Signal Transduction* **2012**, No. ID248759.

(13) Morales-Avila, E.; Ferro-Flores, G.; Ocampo-Garcia, B. E.; Gomez-Olivan, L. M. *J. Biomed. Nanotechnol.* **2012**, *8*, 991−999.
(14) Kang, S. M.; Kim, T. H.; Choi, J. W. *J. Nanosci. Nanotechnol.* **2012**, *7*, 5185−5190.
(15) Lee, S. M.; Kim, H. J.; Ha, Y. J.; Park, Y. N.; Lee, S. K.; Park, Y. B.; Yoo, K. H. *ACS Nano* **2013**, *7*, 50−57.
(16) Cohen-Karni, T.; Jeong, K. J.; Tsui, J. H.; Reznor, G.; Mustata, M.; Wanunu, M.; Graham, A.; Marks, C.; Bell, D. C.; Langer, R.; Kohane, D. S. *Nano Lett.* **2012**, *12*, 5403−5406.
(17) Siow, K. S.; Britcher, L.; Kumar, S.; Griesser, H. J. *Plasma Processes Polym.* **2006**, *3*, 392−418.
(18) Antunes, J. M.; Fernandes, J. V.; Sakharova, N. A.; Oliveira, M. C.; Menezes, L. F. *Int. J. Solids Struct.* **2007**, *44*, 8313−8334.
(19) Antunes, J. M.; Menezes, L. F.; Fernandes, J. F. *Int. J. Solids Struct.* **2007**, *44*, 2732−2747.
(20) Jie-Rong, C.; Wakida, T. *J. Appl. Polym. Sci.* **1997**, *66*, 1733−1739.
(21) Li, L.; Jones, P. M.; Hsia, Y. *Appl. Surf. Sci.* **2011**, *257*, 4478−4485.
(22) Miyake, S.; Shindo, T. *Thin Solid Films* **2013**, *527*, 210−221.
(23) Tak, Y.; Kim, K.; Park, H.; Lee, K.; Lee, J. *Thin Solid Films.* **2002**, *411*, 12−16.
(24) Liu, F.; Shang, S.; Duan, Y.; Li, L. *J. Appl. Polym. Sci.* **2012**, *123*, 2800−2804.
(25) Jafari, R.; Farzaneh, M. *Appl. Phys. A: Mater. Sci. Process.* **2011**, *102*, 195−199.
(26) Drabik, M.; Polonskyi, O.; Kylian, O.; Cechvala, J.; Artemenko, A.; Gordeev, I.; Choukourov, A.; Slavinska, D.; Matolinova, I.; Biederman, H. *Plasma Processes Polym.* **2010**, *7*, 544−551.
(27) Vogler, E. A. *Adv. Colloid Interface Sci.* **1998**, *74*, 69−117.
(28) Piedade, A. P.; Nunes, J.; Vieira, M. T. *Acta Biomater.* **2008**, *4*, 1073−1080.
(29) Wong, S. Y.; Han, L.; Timachova, K.; Veselinovic, J.; Hyder, M. N.; Ortiz, C.; Klibanov, A. M.; Hammond, P. T. *Biomacromolecules* **2012**, *3*, 719−726.
(30) Palumbo, F.; Mundo, R. D.; Cappelluti, D.; d'Agostino, R. *Plasma Processes Polym.* **2011**, *8*, 118−126.
(31) Nunes, J.; Santos, R. J.; Loureiro, V.; Piedade, A. P. *Plasma Processes Polym.* **2012**, *9*, 709−717.
(32) Werner, C.; Konig, U.; Augsburg, A.; Arnhold, C.; Korber, H.; Zimmermann, R.; Jacobasch, H. *Colloids Surf., A* **1999**, *159*, 519−529.
(33) Cai, K.; Frant, M.; Bossert, J.; Hildebrand, G.; Liefeith, K.; Jandt, K. D. *Colloids Surf., B* **2006**, *50*, 1−8.
(34) Berlind, T.; Tengvall, P.; Hultman, L.; Arwin, H. *Acta Biomater.* **2011**, *7*, 1369−1378.
(35) Puskas, J. E.; Dahman, Y.; Margaritis, A. *Biomacromolecules* **2004**, *5*, 1412−1421.
(36) Sivaraman, B.; Fears, K. P.; Latour, R. A. *Langmuir* **2009**, *25*, 3050−3056.
(37) Szott, L. M.; Horbett, T. A. *Curr. Opin. Chem. Biol.* **2011**, *15*, 677−682.
(38) Bhushan, B.; Utter. *J. Colloids Surf., B* **2013**, *102*, 484−491.
(39) Du, W.; Wang, Y. *J. Appl. Polym. Sci.* **2013**, *127*, 4256−4261.
(40) Jachimska, B.; Pajor, A. *Bioelectrochemistry* **2012**, *87*, 138−146.
(41) Haynes, C. A.; Norde, W. *Colloids Surf., B* **1994**, *2*, 517−566.
(42) Matsumura, H.; Kawasaki, K.; Okumura, N.; Kambara, M.; Norde, W. *Colloids Surf., B* **2003**, *32*, 97−103.